Energy band edge alignment of anisotropic BiVO$_4$ to drive photoelectrochemical hydrogen evolution

Chang Woo Kim [a], Sohyun Ji [b], Myung Jong Kang [b], Hongryeol Park [b], Feng Li [c], Hui-Ming Cheng [c], Young Soo Kang [b, *]

[a] Department of Graphic Arts Information Engineering, College of Engineering, Pukyong National University, Busan, 48513, Republic of Korea
[b] Korea Center for Artificial Photosynthesis and Department of Chemistry, Sogang University, #1 Shinsu-dong, Mapo-gu, Seoul, 121-742, Republic of Korea
[c] Shenyang National Laboratory for Materials Science, Institute of Metal Research, Chinese Academy of Sciences, Shenyang, 110016, China

ARTICLE INFO

ABSTRACT

Bismuth vanadate (BiVO$_4$) has been highlighted as the most efficient photoanode light absorber for the solar light-driven water oxidation reaction despite the lack of fundamental understanding of its poor performance. Though the BiVO$_4$ performance has been significantly improved, the underlying reasons for this performance are not well understood. Here, anisotropically grown BiVO$_4$ is designed to achieve band edge engineering induced by coupled crystal facets for hydrogen evolution reaction (HER), which is not possible with isotropic BiVO$_4$ powder suspension. HER performances depending on the exposure area of the crystal facets in the anisotropic BiVO$_4$ are investigated using electronic conduction and in situ X-ray absorption spectroscopy during HER. Our results reveal that the nature of the exposed area of the optimized coupled crystal facets in a BiVO$_4$ photoelectrode critically dominates the surface charge density and conductivity, efficiently driving the HER. Sequentially, coupling between different crystal facets of BiVO$_4$ photoelectrode led energy band edge to be upward. The results show that the energy band edge alignment tuned by coupled crystal facet can be applicable to other inorganic photocatalyst/ photoelectrodes to promote efficient artificial photosynthetic reactions.

© 2019 Elsevier Ltd. All rights reserved.

1. Introduction

Artificial photosynthesis is a conversion process for generating sustainable chemical fuels by utilizing solar light [1—3]. Solar light-driven water splitting is one of the most attractive routes for artificial photosynthesis [4—6]. Solar fuel production has been approached via photoelectrochemical (PEC) systems since the first report of the Honda-Fujishima effect in 1972 [7]. Compared with photochemical (PC) reactions using a powder suspension system, the configuration of a PEC water splitting system principally comprises a solar light absorber and a counter electrode within the electrolyte [8]. Reduction/oxidation reactions of H$_2$O molecules are involved at the electrode-electrolyte interface in the two physically separated compartments [9]. To achieve efficient reduction/oxidation reaction in a PEC system, tremendous amount of research have been dedicated to the study of the fundamentals of photon absorption, charge carrier separation, carrier diffusion, carrier

transport, catalytic efficiency and mass transfer as the so-called six gear parameters [10,11]. Advances in PEC artificial photosynthesis have revealed that the combination of these six fundamental parameters determines the overall efficiency of solar fuel production. Pioneering research on semiconductor/co-catalyst interfaces reported by Can Li et al. [12], the introduction of a dual-layer oxidation co-catalyst by Kim and Choi [13], a dual-absorber tandem cell by Sivula et al. [14], and use of plasmonic-metal nanostructures by Wu et al. [15] have provided a basis for understanding the significance of these fundamental parameters.

The basic aspects of a photoelectrode are light harvesting, charge separation via diffusion and charge collection. Therefore, new concepts for metal oxides have been designed and guided by simulations. The strategies for band-structure tailoring [16—18], crystal facet engineering [19], and morphology structuring [20] have been used to satisfy the thermodynamic and kinetic requirements for performance improvement. These suggestions, such as interstitial/substitutional doping of elements and crystal cuts on TiO$_2$, ZnO, Cu$_2$O, WO$_3$ and SrTiO$_3$ have been mostly studied for PC systems instead of PEC systems. In particular, bismuth vanadate

* Corresponding author.
E-mail address: yskang@sogang.ac.kr (Y.S. Kang).

(BiVO$_4$) with a monoclinic scheelite structure has been used for the visible light-triggered water oxidation reaction since the landmark research of Kudo et al. [21] and Lee et al. [22]. From the introduction of impurity elements, surface modifications, and coupling with graphitic carbon materials, to the post-synthetic treatments, tremendous efforts on BiVO$_4$ have been made to overcome its intrinsic shortcomings, such as poor charge transfer kinetics [23—25]. Although, extensive research has been carried out on photocatalytic improvements, there is still great potential for performance improvements. Even though BiVO$_4$ has been adopted in PEC systems, it has been solely classified as a photon absorber [26].

In our previous work, we investigated, for the first time, the introduction of (040) crystal facet-engineered BiVO$_4$ photoanode for oxygen evolution reaction (OER). Our designed model of the BiVO$_4$ photoanode with selectively exposed (040) crystal facets demonstrated the significance of charge separation efficiency and surface charge transfer efficiency induced by the (040) plane in a pure BiVO$_4$ photoanode, resulting in the highest PEC performance [27,28]. Our findings suggest that the method of exposing the photoactive (040) crystal facets of the BiVO$_4$ photoanode should be applicable to other metal oxide photoelectrodes. Strikingly, here, anisotropically grown BiVO$_4$ photoelectrode is designed to achieve band edge engineering induced by coupled crystal facets for photoelectrochemical hydrogen evolution reaction (HER) even though intrinsic performances in BiVO$_4$ corresponds to OER. Given that artificial photosynthesis occurs in the presence of an electrolyte, another significant aspect is the interfacial phenomena between the metal oxide solid surface and a liquid electrolyte during the HER. Understanding the nature of the interfacial surface structure at the atomic level and molecular scale during the photon conversion process is crucial for practical applications. Observation of these *in situ* phenomena through *ex situ* characterization in air requires one to be very careful, resulting in a considerable debate on the subject. To meet this challenge, we employed *in situ* PEC X-ray absorption spectroscopy (XAS), which is a straight-forward method for unravelling the chemical and structural significance of interfacial surface structure of coupled crystal facets in solar light illumination under electrochemical control. Herein, we provide scientific aspects of electronic conduction and surface charge density using the relative exposure extent of coupled crystal facets for HER in BiVO$_4$, which is the essential first step toward improving PEC performances.

2. Experimental section

2.1. Electrode preparation

The synthesis procedure for scheelite monoclinic bismuth vanadate (BVO) was slightly modified from that described in our previous report [27,28]. For the BVO seed layer, Bi(NO$_3$)$_3$•5H$_2$O (5 mmol, 2.4254 g, Sigma-Aldrich, 98%), NH$_4$VO$_3$ (5 mmol, 0.5849 g, Sigma-Aldrich) and citric acid (2-hydroxypropane-1,2,3-tricarboxylic acid, 10 mmol, Daejung, Monohydrate 99.5%) were dissolved in 15 mL of 23.3% aqueous HNO$_3$ (v/v of 60% HNO$_3$ and distilled water, 0.63/1) and stirred for 30 min. The transparent blue solution was added to acetic acid (3.75 mL) with polyvinyl alcohol (PVA, 1.2 g, Aldrich, Mw 89000—98000, 99+% hydrolyzed) and stirred vigorously until the solution became transparent, for approximately 6 h. After the FTO substrate (TEC-8, 6—9 Ω/sq., 2.0 cm × 2.0 cm) was cleaned using a distilled water, acetone and 2-propanol (v/v/v, 1/1/1) solution for 30 min and dried with nitrogen gas, the as-prepared blue solution was dropped and spin-coated onto a clean FTO substrate at 1000 rpm for 10 s and 2000 rpm for 10 s followed by heat treatment in air at 723 K for 4 h. For the anisotropically-grown BVO photoelectrode, Bi(NO$_3$)$_3$•5H$_2$O

(4 mmol, 0.1164 g) and NH$_4$VO$_3$ (4 mmol, 0.028 g) were dissolved in 60 mL of 2.0 M aqueous HNO$_3$. Then, as a structure-directing agent, a titanium (III) chloride solution (Sigma-Aldrich, ≥12% TiCl$_3$ basis) was added to the as-prepared solution. After adjusting the pH to 1.0 using an ammonia solution (NH$_4$OH, JIN Chemical, 25—28 wt%), the reaction solution was transferred to a Teflon-lined autoclave. The pre-fabricated BVO seed layer on the FTO substrate was immersed in the reaction solution and allowed to react at 150 °C for 10 h. The hydrothermally reacted substrate was then heat-treated at 773 K for 4 h. For the manipulation of the exposure ratio of crystal facets of the BVO photoelectrode, the amount of TiCl$_3$ solution was adjusted by adding 0.140, 0.180, 0.268 and 0.320 mL of the TiCl$_3$ solutions and were denoted as $_{14}$BVO, $_{18}$BVO, $_{26}$BVO and $_{32}$BVO, respectively.

2.2. Materials characterization

The surface crystal structures of individual facet on BiVO$_4$ were simulated by the Crystal MakerTM software. The crystallographic information for the BVO photoelectrode was obtained using X-ray diffraction (XRD, Rigaku miniFlex-II desktop X-ray diffractometer, Cu Kα radiation with λ = 0.154056 nm). The microscopic observation of the BVO photoelectrode was carried out using SEM (Hitachi S-4300 FE-SEM) equipped with Oxford JEM-2010 energy dispersive spectroscopy (EDS). High resolution TEM images and SAED pattern were obtained using a JEOL transmission electron microscope (JEM 2100F) at an accelerating voltage of 200 keV. Electronic conduction of individual microcrystals of BVO were measured on a scanning electron microscope (FEI, NanoSEM 430) equipped with a four-probe micromanipulator (Kleindiek MM3A-EM) in its vacuum chamber at room temperature. A silicon wafer was used as a substrate to support individual microcrystals from scratched samples of the BVO photoelectrode, which were ultrasonically dispersed in an ethanol solution prior to dropping onto the substrate. For moving the microcrystal and measuring its I—V curves, two tungsten probes were connected to a Keithley 4200-SCS semiconductor characterization system. Prior to measurement, two tungsten probes were manipulated to achieve tip-to-tip contact and then subjected to Joule heating by applying a scanned voltage from 0 to 10 V several times to fully remove the surface tungsten oxide layer on the probes. To determine the valence band minimum (VBM), the valence band position was determined by ultraviolet photoelectron spectroscopy (UPS, AXIS Nova KRATOS Inc.) using He I (21.22 eV) excitation with a constant pass energy of 5 eV in an ultrahigh vacuum (UHV). The optical absorption and transmittance of the thin BVO film were measured using a Varian Cary 5000 UV—Vis—NIR Spectrophotometer (Agilent Technologies).

2.3. Time Resolved Photoluminescence Measurement

An inverted-type scanning confocal microscope (Picoquant Micro-Time-200) at Korea Basic Science Institute (Daegu) was employed to obtain 2D mapping images and decay curves of the time-resolved photoluminescence (TRPL) of the BVO photoanodes. A 375 nm single-mode pulsed diode laser with a pulse width of 240 ps and a 10 MHz repetition rate was employed as the excitation source, and an average power of <1 μW was used. The emissions from the BVO photoanodes were collected with a dichroic mirror (AHF Z375RDC), a long-pass filter (AHF HQ405lp), a 50 μm pinhole, and a single-photon avalanche diode (SPAD) after passing through the neutral density filter, in which the photon counting rate was maintained at approximately 1% of the excitation rate. The data acquisition was based on a time correlated single photon counting technique. The measured TRPL data were

viewed in the SymPhoTime operating software (ver. 5.1.3). The lifetime values were averaged as "intensity weighted lifetimes" for many samples. For each sample, we estimated the average lifetime from the TRPL images by measuring five or more BVO photoanodes.

2.4. Photoelectrochemical Measurements

A 300 W Xe arc lamp was used for simulated solar illumination with an AM 1.5G filter (Asahi HAL-320, 100 mW cm^{-2}). Prior to the PEC measurement, the power density of the incident light was adjusted to 100 mW cm^{-2} using an NREL certified reference cell (Photo Emission Tech., Inc.). The illumination was set as a backside illumination to the FTO surface. The illuminated area was 0.636 cm^2 of a circle with a diameter of 0.9 cm in 4 cm^2 of the BVO photoelectrode. The photoelectrochemical measurements of the BVO photoanodes as working electrodes in a conventional three-electrode system were performed using a PL-9 potentiostat with and without the simulated solar light illumination. Using a Pt electrode and Ag/AgCl reference electrode in an aqueous Na$_2$SO$_4$ solution (0.5 M, pH = 6.8), the I–V curves were plotted at a scan rate of 20 mV s^{-1} by sweeping the potential in the positive direction.

The light harvesting efficiency (LHE) at each wavelength was calculated from the absorbance using the following equation [13,29].

LHE = $1-10^{-A(\lambda)}$ (A(λ): absorbance at wavelength λ)

The incident photon to current conversion efficiency (IPCE) from 300 to 600 nm was determined with an applied potential of 0.3 V (vs Ag/AgCl) using a specially designed IPCE system (PV Measurements, Inc.). An Oriel Cornerstone 130 monochromator was used to produce monochromatic light with an interval of 10 nm. Based on the LHE and IPCE, the absorbed photon-to-current efficiency (APCE) was determined at each wavelength using the following equation [11,13,29].

APCE (%) = IPCE (%) / LHE

All of the PEC measurements were performed using a Ag/AgCl (2.0 M of KCl) reference electrode at room temperature, and then, the applied bias was converted to the reversible hydrogen electrode (RHE) using the following Nernst equation:

E$_{RHE}$ = E$_{Ag/AgCl}$ + E$^o_{Ag/AgCl\ vs.\ NHE}$ +0.0591 V × pH

(E$^o_{Ag/AgCl\ vs.\ NHE}$ = 0.1976 V vs. NHE at 25 °C)

where E$_{RHE}$ is the potential vs. RHE, 0.0 V vs. RHE for water oxidation, E$_{RHE}$ is the experimental potential measured vs. the Ag/AgCl reference electrode, and E$^o_{Ag/AgCl\ vs.\ NHE}$ is the standard potential of the Ag/AgCl vs. NHE (0.1976 V at 25 °C).

2.5. Hydrogen Evolution Measurements

The hydrogen evolution experiments were carried out in an airtight continuous flow cell connected to an online GC system (Agilent 7890A) equipped with HP-Molesieve GC column (30 m × 0.53 mm). A 50 mL cell with 50 mL of 0.5 M Na$_2$SO$_4$ aqueous solution containing 0.1 g of $_{26}$BVO was illuminated. After Ar gas (99.9999%) was used at a flow rate 6 mL min^{-1} for 3 h to remove the air under dark conditions, the reactor was illuminated under a continuous flow of Ar (6 mL min^{-1}).

2.6. In situ PEC-X-Ray Absorption Analysis

X-ray absorption analysis of the BVO photoelectrode was carried out with the PEC measurement. The PEC cell was set according to the previously mentioned conditions. The local bonding structure of BVO in a 0.5 M Na$_2$SO$_4$ (pH 6.8) electrolyte with a potentiostat (Ivium compactstat) was measured using X-ray Absorption Structure (XAFS) with a synchrotron radiation beam at the Pohang Accelerator Laboratory (PAL) 10C beam line. Dark conditions with external bias potential and illumination-on with 0.6 V external bias potential versus Ag/AgCl reference electrode were employed. The measured XAS data have been refined into X-ray absorption near edge spectra (XANES) and extended X-ray absorption fine structure (EXAFS), and fitted by computational calculations using the IFEFFIT algorithm (Supporting Information).

3. Results and discussion

To determine the nature of the interfacial surface structure at the atomic level, the exposure ratio of crystal facets of a monoclinic scheelite BiVO$_4$ (BVO) photoanode was designed to achieve enhancing PEC OER performances induced by the crystal facets [28]. Based on our recent work, anisotropic BVO single crystals were hydrothermally grown from their seed layer on a fluorine-doped tin oxide (FTO) substrate. Microscopic observations provided information about the exposure of the relative {010} and {110} crystal facet ratio in an anisotropic BVO single crystal film (Fig. 1), in which the relative exposure extent of their crystal facets was manipulated by adding 0.140 mL ($_{14}$BVO, black square), 0.180 mL ($_{18}$BVO, green square), 0.268 mL ($_{26}$BVO, red square) and 0.320 mL ($_{32}$BVO, blue square) of the structure directing agent. Typical top-view scanning electron microscopy (SEM) images show that the relative extent of the laterally-exposed (040) crystal facet increased as the amount of the structure directing agent increased. Cross-sectional SEM images and selected area electron diffraction (SAED) patterns obtained by using high-resolution transmission electron microscopy (HRTEM) showed that the BVO microcrystal grew anisotropically from the BVO seed layer on the FTO. To better understand the crystal structure of the $_{26}$BVO microcrystal plate with the elemental mapping images (supporting information. Fig. S1), its X-ray powder diffraction (XRD) pattern was well indexed to monoclinic scheelite BiVO$_4$ (JCPDS card #140688, space group: I2/a), in which the growth direction from the BiVO$_4$ seed layer was along the [121] and [110] directions in the monoclinic structure, determined using XRD (Fig. S2). Among all diffraction peaks in XRD, a dominant peak corresponds specific orientation of the film [30]. The relative intensity between (110), (121) and (040) indicates that the exposed extent of each facet depends on the amount of structure directing agent. Using the 2θ peak position (30.8°) of the (040) plane in the XRD pattern and the (040) plane in the SAED pattern (yellow square of Fig. 1), representative individual microcrystals in $_{26}$BVO were observed as a single crystal plate with 6-{110} crystal facets surrounding 2-{010} crystal facets (violet square in Fig. 1). From the calculation of the optical absorbance (Fig. S3), the solar light harvesting efficiency (LHE) in $_{18}$BVO, $_{26}$BVO and $_{32}$BVO was found to be 90% between 375 and 485 nm (Fig. 2a). Although it is presumed that about 80% of LHE would be induced by the relatively thin film of $_{14}$BVO, it is worth noting that the morphologies in our BVO photoelectrode were not dominant factors for the LHE. In particular, from the observation of λ_{max} at 400 nm for $_{26}$BVO, it is clear that the incident photon-to-current conversion efficiency (IPCE) of the LHE is very different from that of the powder suspension. The IPCE of $_{26}$BVO reached 28%, which was the highest value observed compared to 23% and 21% for $_{32}$BVO and in $_{18}$BVO, respectively, at a bias potential of 0.9 V (vs. RHE) (Fig. 2b). The
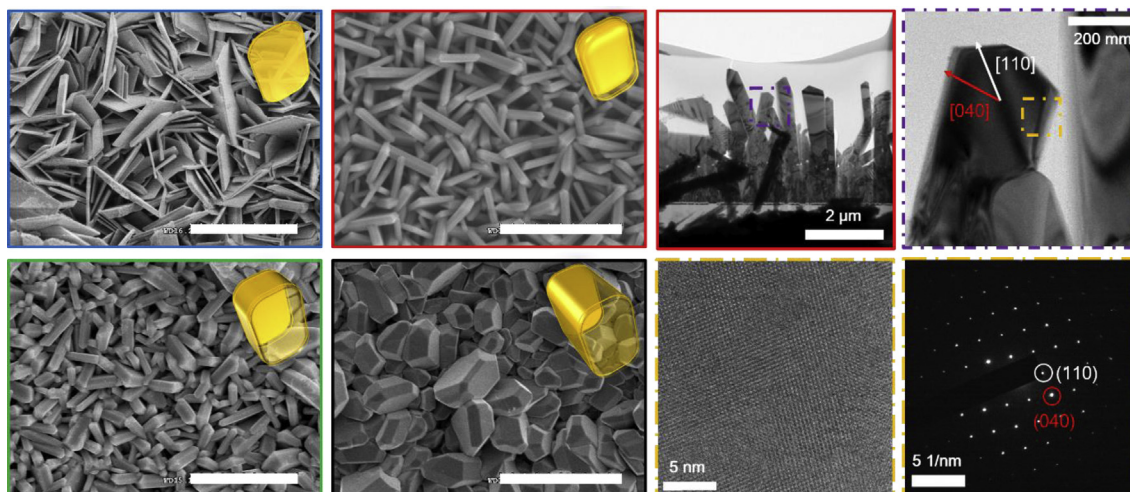
Fig. 1. Schematic representation and microscopic observations. Schematic representation and typical top-viewed SEM images of $_{14}$BVO (black square), $_{18}$BVO (green square), $_{26}$BVO (red square) and $_{32}$BVO (blue square). Focused ion beam-treated cross sectional HRTEM image (red and violet square) and SAED pattern (yellow square) of individual $_{26}$BVO microplate. From the microscopic images, an exposure ratio of crystal facets was manipulated in BVO photoelectrode. White scale bar in SEM images is 5 μm.
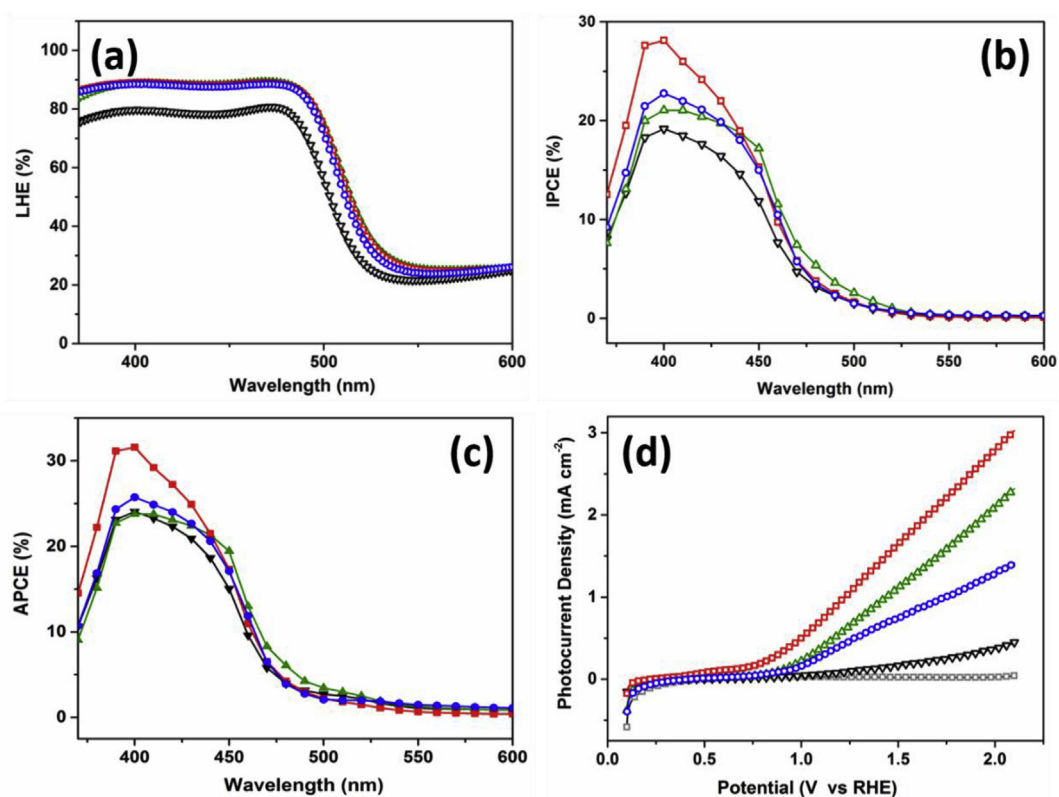
Fig. 2. PEC characteristics. (a) LHE, (b) IPCE, (c) APCE and (d) I–V behavior of BVO photoelectrode, $_{14}$BVO (black), $_{18}$BVO (green), $_{26}$BVO (red) and $_{32}$BVO (blue). PEC performances of $_{26}$BVO indicate that the exposure ratio of crystal facets is dominant to control η_{sep} and η_{trans}.

absorbed photon-to-current conversion efficiency (APCE) was 32% in $_{26}$BVO at 0.9 V (vs. RHE) (Fig. 2c). IPCE (%) is typically calculated by multiplying the charge separation efficiency (η_{sep}), charge transport efficiency (η_{trans}) and interfacial charge transfer efficiency (η_{inter}) at the interfacial solid-liquid junction [11,29]. Given that η_{inter} of BVO, of which the LHE was constant, is dominated by the introduction of the co-catalyst, these IPCE and APCE characteristics are consistent with the fact that the specific ratio of the coupled crystal facets led to higher values of η_{sep} and η_{trans}.

As expected from the coupled exposure of crystal facets with different extent of {010} and {110}, the PEC characteristics shown in Fig. 2d indicate that $_{26}$BVO produced the highest photocurrent density of 3.0 mA cm^{-2}, which was much larger than that of $_{18}$BVO (2.3 mA cm^{-2}) and $_{32}$BVO (1.4 mA cm^{-2}) at 2.1 V (vs. RHE) under AM 1.5 G illumination. $_{14}$BVO exhibited an onset potential (V$_{op}$) of 0.42 V, which is typically observed in bulk BiVO$_4$. Interestingly, V$_{op}$ exhibited a cathodic shift to 0.22 V for $_{26}$BVO. The obtained photocurrent responses in the chopped light current-voltage (I–V)

curve indicate that $_{26}$BVO overcome an electron-hole recombination at the electrode/electrolyte interface (Fig. S4). Considering that the I—V characteristics of $_{14}$BVO showed an inherent behavior of typical BiVO$_4$ suffering from slower charge mobility and lesser charge separation than the others [31,32], it is important to note that the specific exposure degree of the crystal facets drive the photogenerated charge flow and enhance η_{sep} and η_{trans}. More interestingly, cathodic current was observed below V_{op} in $_{26}$BVO, even BiVO$_4$ is well-known n-type semiconducting material (Fig. S4). In addition, even though $_{32}$BVO and $_{18}$BVO had similar LHE, IPCE and APCE values, their photocurrent densities were remarkably different. This result indicates that the relative exposure of the coupled crystal facet was favorable for the lower energy barrier for η_{sep} and η_{trans}. To a significant extent, such enhanced PEC characteristics of the excitation and decay kinetics of the photogenerated charge carriers were confirmed using time-resolved photoluminescence (TRPL) spectroscopy of the BVO surface at room temperature (RT). 2D-PL images and TRPL decay curves of four types of BVO photoelectrodes proved the information about the relative numbers of the excited state electrons and their charge recombination rates and decay times, indicating that the accumulation of photogenerated charges at the surface drives the water oxidation kinetics. Using the excitation wavelength at 375 nm, the average decay times (τ_{ave}) of the charge carriers in $_{14}$BVO, $_{18}$BVO and $_{26}$BVO were determined to be 21, 25, and 30 ns, respectively, as shown in Fig. 3. The τ_{ave} value of the charge carriers in the $_{32}$BVO photoelectrode was enhanced by 38 ns compared with those of the others, which indicates that the larger exposure area of

the {010} crystal facet increased the charge transfer efficiency. Additionally, the energy barrier for charge transfer was investigated with the electrical conductivity of BVO with different exposure extent of coupled crystal facets, as shown in Fig. 3. An Individual BVO microcrystal with different exposure ratios of crystal facets was electrically connected to tungsten (W) tips, the probe station of which was situated in a field emission scanning electron microscopy (FE-SEM). The electrical conductivities along the [010] direction of the BVO samples with different area ratios of crystal facets were determined to be between 2.0 and −2.0 V after removing surface oxides of the W tips by Joule heating through the W tip-to-tip contact (Fig. S5). The nonlinear current curve increased as the applied bias potential increased in the representative BVO curve, indicating the presence of a Schottky barrier at the interface between the metal tips and metal oxide [33,34]. Such a potential barrier formed at the interface corresponds to a difference in the work function between the BiVO$_4$ metal oxide (~5.27 eV) [35] and W metal probes (~4.55 eV) [34]; the difference between the Fermi and vacuum energies is discussed later using UV photoelectron spectroscopy (UPS) investigation results. The electrical connection between the {010} facets of $_{14}$BVO was non-conductive. The contact current between the {010} facets of the $_{18}$BVO microcrystals was ca. 7.5 nA at −2.0 V. The highest current was observed to be ca. 12 nA in the electrical connection between the {010} facets of the $_{26}$BVO microcrystal. The current of $_{26}$BVO was approximately 4.8 times higher than that of $_{32}$BVO, the surface current of which was ca. 2.5 nA at a bias potential between −2 and 2 V. As expected from previous reports, the exposure of specific crystal facets has been
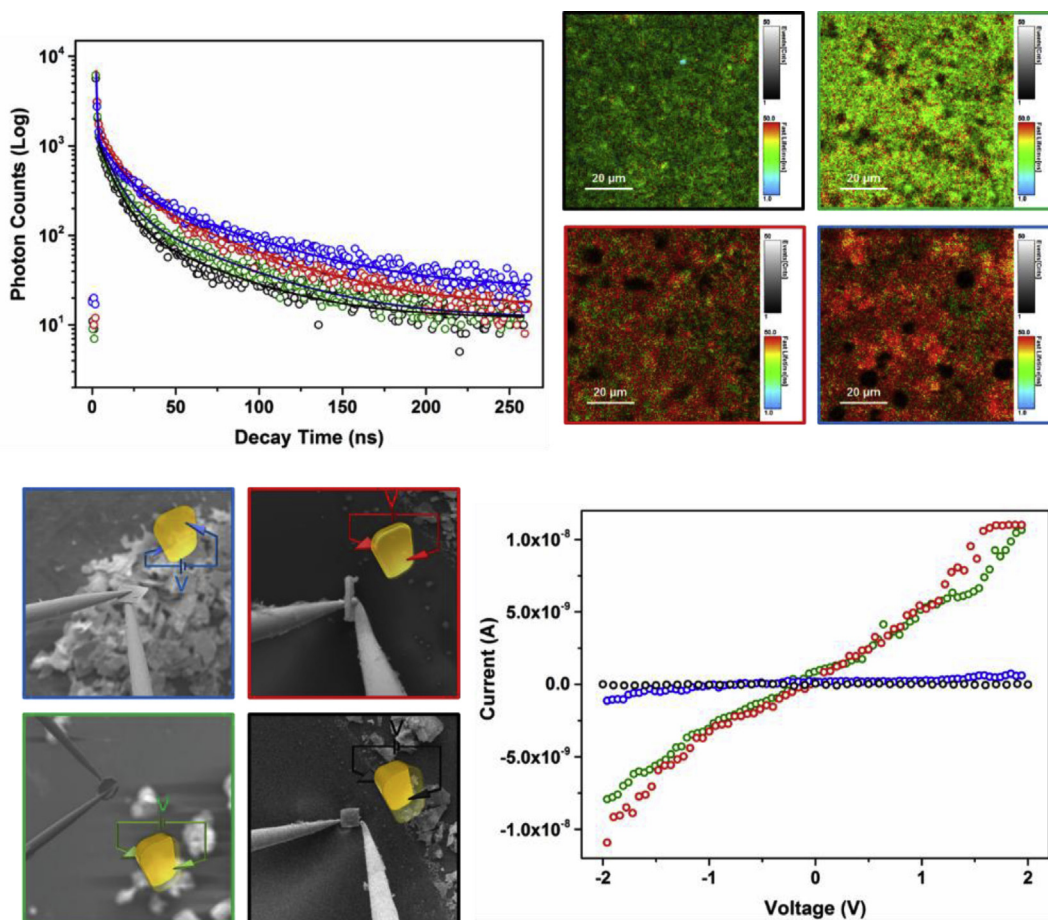

Fig. 3. Time-resolved photoluminescence and electrical conduction. Time-resolved photoluminescence (TRPL) and 2D-PL decay images (upper row) and electrical conduction measurement of individual BVO situated in SEM chamber (lower row), $_{14}$BVO (black), $_{18}$BVO (green), $_{26}$BVO (red) and $_{32}$BVO (blue).

recognized as the dominant factor for manipulating the photo-catalytic/photochemical performance. Because the {010} facets were electrically connected in the all scheelite monoclinic structure BVO samples, the contact resistance at the BVO-W interfaces should be constant. Interestingly, the current difference observed in our experiments implies the presence of an alternative factor that enhances the intrinsic conductivity of the metal oxide. This result indicates that the anisotropy of the atomic arrangement results in coupled crystal facet-dependent electrical properties and, simultaneously, the thickness of the surface layer with different exposure extent of the {010} and {110} crystal facets is the unexpected dominant factor for electrical conductivity [34,36]. Although the $_{32}$BVO microcrystal possesses a high exposure of the {010} crystal facet, its current value can be considered as negligible conductivity, like that of $_{14}$BVO, which is clear evidence to support our observation. Our observation that the contact current of the four representative kinds of BVO behaved differently indicates that BVOs with specific exposure extent of coupled crystal facets exert a critical effect on the anisotropic electronic conduction.

For unravelling atomic-level information of the electronic state and local surface structure at BVO interface during the water oxidation reaction, in situ X-ray absorption spectroscopy (XAS) was performed under PEC conditions. As the valence band maximum (VBM) of BVO is determined by the hybrid orbital of Bi 6s/O 2s, Bi in BVO as the X-ray absorbing atom was irradiated by synchrotron X-ray. The fluorescence change was observed for illumination-on and illumination-off conditions to obtain geometric information about the atoms around the Bi atom, as shown in Fig. 4 (a). The X-ray absorption near edge structure (XANES) spectra at the Bi L$_3$-edge of a representative BVO samples were compared for the function of illumination-off (Fig. 4b)/-on (Fig. 4c) conditions. The absorption edge feature of 13430 eV was observed in the XANES spectrum (Fig. S6) [37], which corresponds to electric transition from 2p to 6d based on the selection rules of photon absorption. This feature shows a nearly perfect overlap of all the different BVO samples under illumination-off, even though under illumination-on. This

indicates that the X-ray absorbing atom remains in the Bi^{3+} electronic state under both conditions. It is concluded that the atomic environmental structures of Bi metal in all four kinds of BVO were not influenced by the applied bias potential and illumination, like a previous report on the V atom [31], and produced significant PEC performances. The interatomic distance around the X-ray absorbing Bi atom was investigated with extended X-ray absorption fine structure (EXAFS) spectroscopy under illumination-on and illumination-off conditions. The first oscillation peak centered at 2.44 Å corresponds to the Bi−O distance in BVO at the applied bias potential of 1.2 V. The second oscillation peak at 3.17 Å is associated with the distance between the Bi and V atoms on BVO with an applied bias potential of 1.2 V (Fig. S7). The interatomic distance around the Bi atom of all BVO samples showed negligible changes, regardless of the applied bias potential (Fig. 4d). Interestingly, the illumination-on condition changes the BVO atomic arrangement structure surrounding the Bi atom (Fig. 4e). With the interatomic radial distance between Bi−O at an applied bias potential of 1.2 V under dark conditions as a reference, the distance decreased under the illumination-on condition. The Bi−O distance of 2.44 Å of all the BVO samples under the illumination-off condition decreased to 2.35, 2.30 and 2.25 Å in $_{14}$BVO, $_{18}$BVO and $_{26}$BVO, respectively, under the illumination-on condition (Table S1). The shifts to shorter bond distances under the illumination-on condition indicate increased electron densities of the vacant bonding molecular orbitals of Bi−O, shown by the increased bond order of the Bi−O bond because of the presence of electron-donating species with oxygen such as OH$^-$, O$_2^{*-}$ and H$_2$O. The observed shift by 0.14 Å clearly matches the calculated shift from 2.27 Å to 2.36 Å of the Bi−O geometry reported by Can Li et al. [38], in which spin-polarized density functional theory (DFT) was performed for the excess electrons in BVO, based on a small polaron model [39]. It is worth noting that the changes in the Bi−O bond distances occurred in the order $_{14}$BVO < $_{18}$BVO < $_{26}$BVO, corresponding to the order of increasing PEC performances. On the other hand, the increased interatomic distance of Bi−V from 3.17 Å under dark conditions were in the order 3.21 Å in $_{14}$BVO < 3.28 Å in
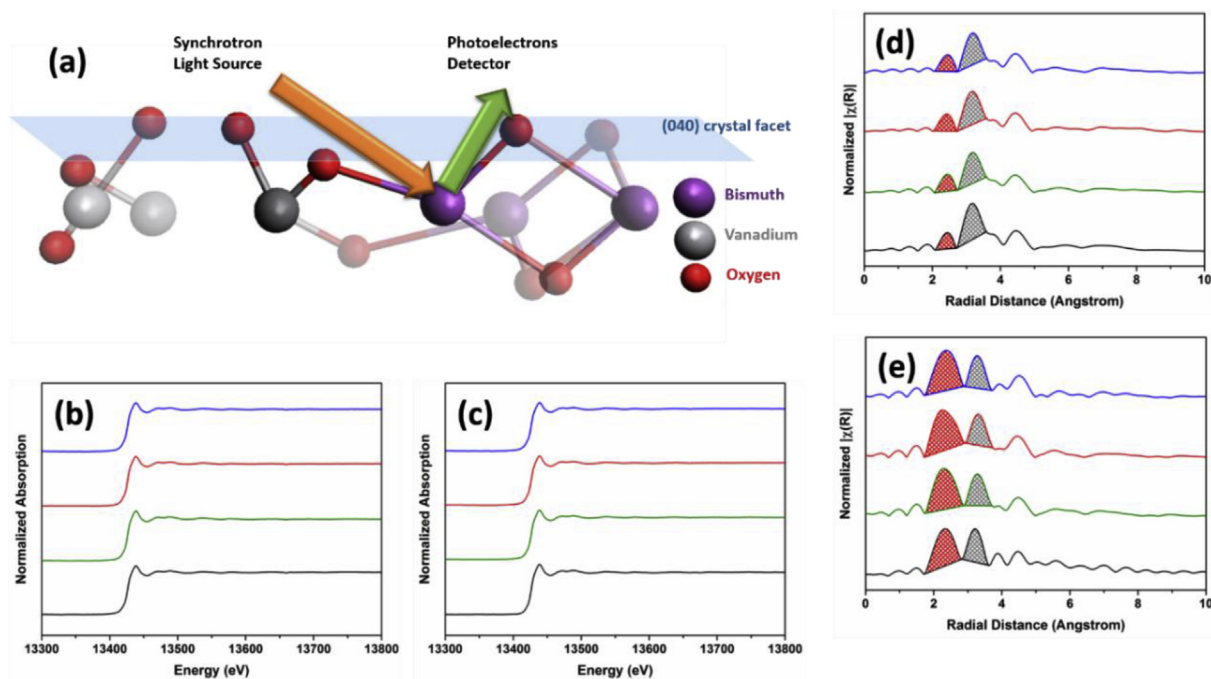

Fig. 4. *In-situ XAS*. (a) Schematic illustration of *in-situ* EXAFS and XANES measured as a function of illumination-off/on. XANES spectrum under illumination-off (b) and illumination-on (c). Bi L$_3$-edge EXAFS measured under illumination-off (d) and illumination-on (e). $_{14}$BVO (black), $_{18}$BVO (green), $_{26}$BVO (red) and $_{32}$BVO (blue). Changes in radial distance and quantitative aspect is remarkable between illumination-off and -on.
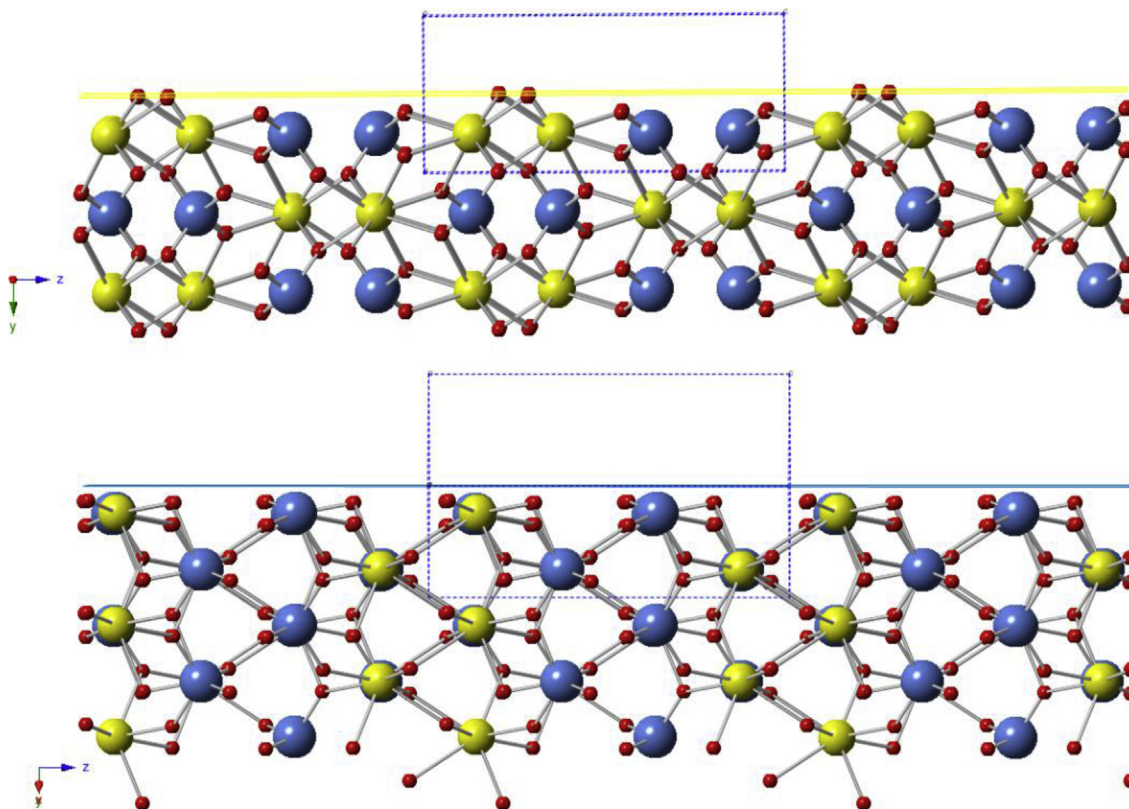
Fig. 5. Geometrical surface structure of BVO. (040) crystal facet of BVO (upper) and (110) crystal facet of BVO (lower). Bi atom (yellow ball), V atom (blue ball) and O atom (red ball).

$_{18}$BVO < 3.30 Å in $_{26}$BVO, indicating that the electron density between the Bi—V bond decreased because of electron donation to water oxidation reaction sites. Our *in situ* PEC-XAS results show that the scientific results obtained for the water splitting reaction at the {010}-{110} coupled crystal facets of BVO are significant. The contribution of electron transfer by Bi 6s orbitals to V 3d orbitals of the conduction band minimum (CBM) of BVO by photoexcitation, in which Bi^{3+} is expected to be oxidized, differs from our observation
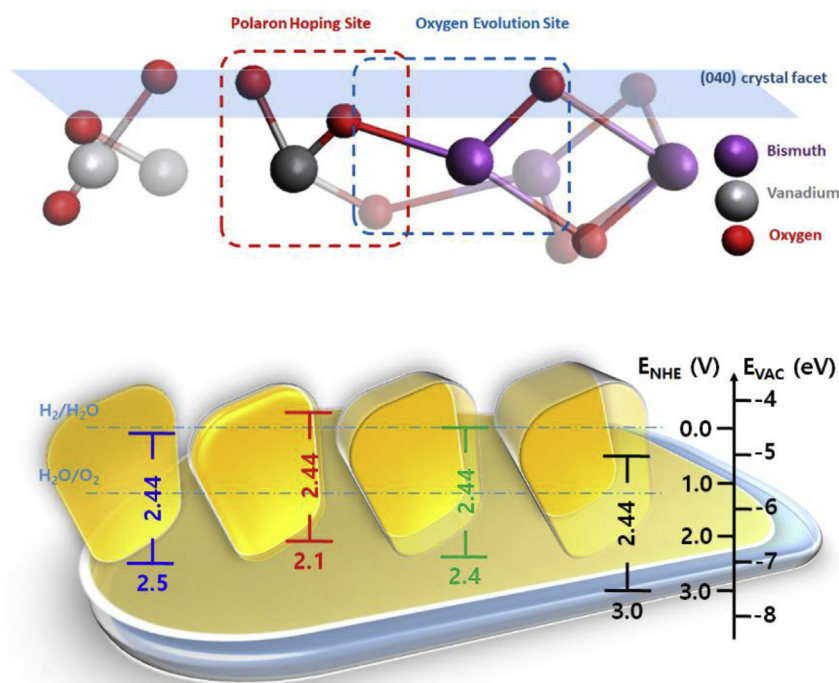

Fig. 6. Schematic illustration of energy band up-lifting. Polaron hoping site and oxygen evolution site on {010} facets on BVO (upper) and calculated energy band edge of $_{14}$BVO (black), $_{18}$BVO (green), $_{26}$BVO (red) and $_{32}$BVO (blue). Energy band edge was up-shifted as exposure extent of coupled crystal facets.

of no shift in the Bi oxidation state based on XANES results. Contraction of the B—O distance and elongation of the B—V distance reveal that the Bi atom fluctuated/oscillated around VO_4^{3-} units under the illumination-on condition. Such oscillations of the Bi atom were quantitatively more predominant in $_{26}$BVO than the other as well (determined using the areas under parabolas in EXAFS). Considering simulated results by Can Li et al., who showed that electron mobility was a {010}-dependent feature and hole mobility was {110}-dependent [40], it can be deduced that a larger number of Bi atoms are able to more freely oscillate in the {010}-{110} crystal facets of $_{26}$BVO than in the other samples. Combining this with the TRPL results, the geometrical atomic structure of $_{26}$BVO facilitates charge carrier polaron formation, and the excess electrons are stabilized at the VO_4^{3-} site and holes are localized at O sites of the BiO_8 unit (Fig. 5). The contraction of the B—O distance is induced by stronger hybridization between Bi 6s and O 2p orbitals, and change in the charge density results in the shifting of band energy. To probe our hypothesis, BVO samples with different extent of exposed crystal facets were investigated for band energy position using the Tauc equation (Fig. S8) and UPS measurements (Fig. S9) [41]. From diffuse reflectance measurements (DRS), the band gap energies (Eg) were determined to be 2.44 eV for the four kinds of BVO. Based on UPS measurements, the band energy position was determined by Mulliken electronegativity theory and UPS

analysis, as suggested by Prof. Domen [42,43]. The VBM measurements showed band energy positions of 3.06 eV (vs NHE) for $_{14}$BVO, 2.43 eV for $_{18}$BVO, 2.08 eV for $_{26}$BVO and 2.58 eV for $_{32}$BVO (Fig. 6). It is worth noting that the VBM position of $_{26}$BVO is more negative, considering that the VBM of typical $BiVO_4$ is located at ~2.8 eV [35]. Strikingly the band energy position moved upward, as can be seen with the Eg value of 2.44 eV because of the specific extent of the {010}/{110} coupled crystal facets. Based on our calculation of the band energy position (Fig. S10), negative-shifting of VBM occurred in order of $_{14}$BVO < $_{18}$BVO < $_{26}$BVO because of the lower energy barrier between BVO and W, as shown in Fig. 2. Simultaneously, an upward shift of CBM in $_{26}$BVO was sufficient to reach the energy level for hydrogen evolution. Given that the CBM of typical $BiVO_4$ is responsible for the H_2 evolution level, CBM in $_{26}$BVO was more negatively shifted to −0.3 eV. To prove our calculation of the CBM position in BVOs, hydrogen evolution of the BVOs was confirmed with gas chromatography without additives, such as hole/electron scavengers. As expected from our observation of the CBM position in $_{14}$BVO, $_{18}$BVO, and $_{32}$BVO, hydrogen was negligibly detected. Interestingly, the hydrogen evolution rate in $_{26}$BVO was about 0.025 mmol g^{-1} h^{-1} and undetectable in the other samples (Fig. 7). This indicates that our observations on the band energy up-lifting is consistent with the increased electron conduction of individual microcrystals with different coupled exposure extent of crystal facets of BVO. The specific exposure of crystal facets allows band edge engineering of BVO for the entire water splitting reaction, which exerts a considerable influence on electronic conductivity.

4. Conclusion

In summary, the local electronic and geometric atomic crystal structures of BVO with relatively coupled exposure extent of crystal facets were investigated by *in situ* X-ray synchrotron radiation measurements to elucidate the origin of HER performance enhancement. Our findings from the *in situ* PEC-XAS studies showed the contraction of the distance between Bi and O atoms and elongation of the distance of Bi-VO_4 units during the water oxidation reaction. Coupled exposure extent of the {010}/{110} crystal facets caused oscillations of the Bi^{3+} atom and lowered the energy barrier for charge transfer. Through oscillations of the Bi atom, such contraction and elongation could stabilize the holes at oxygen sites and the stabilized holes have a long lifetime that promotes the water oxidation reaction. Based on the above results, it can be clearly concluded that the charge carrier was highly stabilized and stacked and resulted in the up-lifting of the band energy with coupled exposure ratios of {010} and {110} crystal facets. Our findings provide direct evidence of the electronic conductivity and geometric crystal structure of $BiVO_4$ for improved PEC performances at the atomic level, which will help elucidate the mechanism of the water splitting reaction by semiconductor candidates in photovoltaic and photocatalytic reactions.
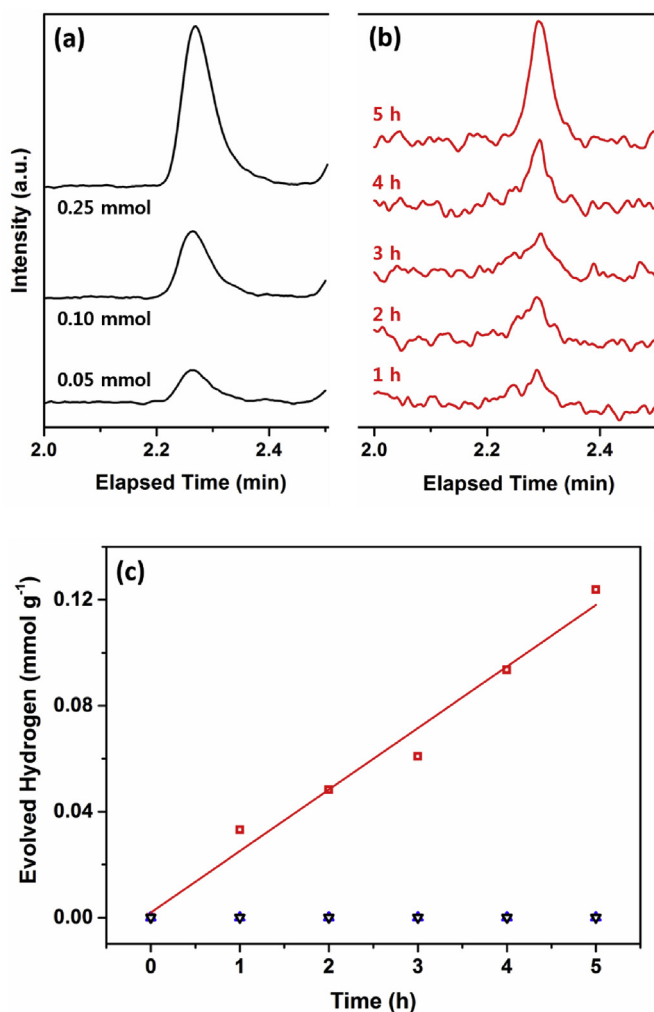
Fig. 7. Evolved hydrogen measurement. (a) Standard calibration of hydrogen, (b) evolved hydrogen of $_{26}$VBO as a function of time and (c) hydrogen evolution curves of $_{14}$BVO (black), $_{18}$BVO (green), $_{26}$BVO (red) and $_{32}$BVO (blue).

References

[1] X.-B. Li, C.-H. Tung, L.-Z. Wu, Semiconducting quantum dots for artificial photosynthesis, Nat. Rev. Chem. 2 (2018) 160–173.

[2] D.G. Nocera, Solar fuels and solar chemicals industry, Acc. Chem. Res. 50 (2017) 616–619.

[3] Y. Tachibana, L. Vayssieres, J.R. Durrant, Artificial photosynthesis for solar water-splitting, Nat. Photon. 6 (2012) 511–518.

[4] K. Sivula, R.V.D. Krol, Semiconducting materials for photoelectrochemical energy conversion, Nat. Rev. Mater. 1 (2016) 15010.

[5] D. Kim, K.K. Sakamoto, D. Hong, P. Yang, Artificial photosynthesis for sustainable fuel and chemical production, Angew. Chem. Int. Ed. 54 (2015) 3259–3266.

[6] X. Chen, S. Shen, L. Guo, S.S. Mao, Semiconductor-based photocatalytic hydrogen generation, Chem. Rev. 110 (2010) 6503–6570.

[7] A. Fusishima, K. Honda, Electrochemical photolysis of water at a semiconductor electrode, Nature 238 (1972) 37–38.

[8] A. Landman, H. Dotan, G.E. Shter, M. Wullenkord, A. Houaijia, A. Maljusch, G.S. Grader, A. Rothschild, Photoelectrochemical water splitting in separate oxygen and hydrogen cells, Nat. Mater. 6 (2017) 646–651.

[9] T.A. Pham, Y. Ping, G. Galli, Modelling heterogeneous interfaces for solar water splitting, Nat. Mater. 16 (2017) 401–408.

[10] K. Takanabe, Photocatalytic water splitting: quantitative approaches toward photocatalyst by design, ACS Catal. 7 (2017) 8006–8022.

[11] T. Yao, X. An, H. Han, J.Q. Chen, C. Li, Photoelectrocatalytic materials for solar water splitting, Adv. Energy Mater. 8 (2018) 1800210.

[12] C. Ding, J. Shi, Z. Wang, C. Li, Photoelectrocatalytic water splitting: significance of cocatalysts, electrolyte, and interfaces, ACS Catal. 7 (2017) 675–688.

[13] T.W. Kim, K.-S. Choi, Nanoporous BiVO₄ photoanodes with dual-layer oxygen evolution catalysts for solar water splitting, Science 343 (2014) 990–994.

[14] J. Brillet, J.-H. Yum, M. Cornuz, T. Hisatomi, R. Solarska, J. Augustynski, M. Graetzel, K. Sivula, Highly efficient water splitting by a dual-absorber tandem cell, Nat. Photon. 6 (2012) 824–828.

[15] J. Li, S.K. Cushing, P. Zheng, F. Meng, D. Chu, N. Wu, Plasmon-induced photonic and energy-transfer enhancement of solar water splitting by a hematite nanorod array, Nat. Commun. 4 (2013) 2651.

[16] C.-Z. Ning, L. Dou, P. Yang, Bandgap engineering in semiconductor alloy nanomaterials with widely tunable compositions, Nat. Rev. Mater. 2 (2017) 17070.

[17] H. Yu, R. Shi, Y. Zhao, T. Bian, Y. Zhao, C. Zhou, G.I.N. Waterhouse, L.-Z. Wu, C.-H. Tung, T. Zhang, Alkali-assisted synthesis of nitrogen deficient graphitic carbon nitride with tunable band structures for efficient visible-light-driven hydrogen evolution, Adv. Mater. 29 (2017) 1605148.

[18] X. Chen, R. Shi, Q. Chen, Z. Zhang, W. Jiang, Y. Zhu, T. Zhang, Three-dimensional porous g-C₃N₄ for highly efficient photocatalytic overall water splitting, Nano Energy 59 (2019) 644–650.

[19] G. Liu, H.G. Yang, J. Pan, Y.Q. Yang, G.Q. (Max) Lu, H.-M. Cheng, Titanium dioxide crystals with tailored facets, Chem. Rev. 114 (2014) 9559–9612.

[20] K.A. Newton, F.E. Osterloh, Size and morphology of suspended WO₃ particles control photochemical charge carrier extraction and photocatalytic water oxidation activity, Top. Catal. 59 (2016) 750–756.

[21] A. Kudo, K. Ueda, H. Kato, I. Mikami, Photocatalytic O₂ evolution under visible light irradiation on BiVO₄ in aqueous AgNO₃ solution, Catal. Lett. 53 (1998) 229–230.

[22] W.J. Jo, H.J. Kang, K.-J. Kong, Y.S. Lee, H. Park, Y. Lee, T. Buonassisi, K.K. Gleason, J.S. Lee, Phase transition-induced band edge engineering of BiVO₄ to split pure water under visible light, Proc. Natl. Acad. Sci. U.S.A. 112 (2015) 13774–13778.

[23] H.L. Tan, R. Amal, Y.H. Ng, Alternative strategies in improving the photocatalytic and photoelectrochemical activities of visible light-driven BiVO₄: a review, J. Mater. Chem. 5 (2017) 16498–16521.

[24] Y. Park, K.J. McDonald, K.-S. Choi, Progress in bismuth vanadate photoanodes for use in solar water oxidation, Chem. Soc. Rev. 42 (2013) 2321–2337.

[25] A.T. Oliveira, M. Rodriguez, T.S. Andrade, H.E.A. de Souza, J.D. Ardisson, H.S. Oliveira, L.C.A. Oliveira, E. Lorencon, A.C. Silva, L.L. Nascimento,

[26] A.O.T. Patrocínio, M.C. Pereira, High water oxidation performance of W-doped BiVO₄ photoanodes coupled to V₂O₅ rods as a photoabsorber and hole carrier, Sol. RRL 2 (2018) 1800089.

[26] X. Shi, I.Y. Choi, K. Zhang, J. Kwon, D.Y. Kim, J.K. Lee, S.H. Oh, J.K. Kim, J.H. Park, Efficient photoelectrochemical hydrogen production from bismuth vanadate-decorated tungsten trioxide helix nanostructures, Nat. Commun. 5 (2014) 4775.

[27] C.W. Kim, M.J. Kang, S. Ji, Y.S. Kang, Artificial photosynthesis for formaldehyde production with 85% of faradaic efficiency by tuning the reduction potential, ACS Catal. 8 (2018) 968–974.

[28] C.W. Kim, Y.S. Son, M.J. Kang, D.Y. Kim, Y.S. Kang, (040)-Crystal facet engineering of BiVO₄ plate photoanodes for solar fuel production, Adv. Energy Mater. 6 (2016) 1501754.

[29] Z. Chen, H.N. Dinh, E. Miller, Photoelectrochemical Water Splitting: Standards, Experimental Methods, and Protocols. Briefs in Energy, Springer-Verlag, New York, 2013.

[30] Y. Han, L. Zhang, Y. Wang, H. Zhang, S. Zhang, Photoelectrocatalytic activity of an ordered and vertically aligned TiO₂ nanorod array/BDD heterojunction electrode, Sci. Bull. 62 (2017) 619–625.

[31] B.J. Trześniewski, I.A. Digdaya, T. Nagaki, S. Ravishankar, I. Herraiz-Cardona, D.A. Vermaas, A. Longo, S. Gimenez, W.A. Smith, Near-complete suppression of surface losses and total internal quantum efficiency in BiVO₄ photoanodes, Energy Environ. Sci. 10 (2017) 1517–1529.

[32] J. Song, M.J. Seo, T.H. Lee, Y.-R. Jo, J. Lee, T.L. Kim, S.-Y. Kim, S.-M. Kim, S.Y. Jeong, H. An, S. Kim, B.H. Lee, D. Lee, H.W. Jang, B.-J. Kim, S. Lee, Tailoring crystallographic orientations to substantially enhance charge separation efficiency in anisotropic BiVO₄ photoanodes, ACS Catal. 8 (2018) 5952–5962.

[33] G. Liu, L.-C. Yin, J. Pan, F. Li, L. Wen, C. Zhen, H.-M. Cheng, Greatly enhanced electronic conduction and lithium storage of faceted TiO₂ crystals supported on metallic substrates by tuning crystallographic orientation of TiO₂, Adv. Mater. 27 (2015) 3507–3512.

[34] C.-S. Tan, S.-C. Hsu, W.-H. Ke, L.-J. Chen, M.H. Huang, Facet-dependent electrical conductivity properties of Cu₂O crystals, Nano Lett. 15 (2015) 2155–2160.

[35] J.K. Cooper, S. Gul, F.M. Toma, L. Chen, P.-A. Glans, J. Guo, J.W. Ager, J. Yano, I.D. Sharp, Electronic structure of monoclinic BiVO₄, Chem. Mater. 26 (2014) 5365–5373.

[36] C.W. Kim, S.J. Yeob, H.-M. Cheng, Y.S. Kang, A selectively exposed crystal facet-engineered TiO₂ thin film photoanode for the higher performance of the photoelectrochemical water splitting reaction, Energy Environ. Sci. 8 (2015) 3646–3653.

[37] Y. Uemura, D. Kido, A. Koide, Y. Wakisaka, Y. Niwa, S. Nozawa, K. Ichiyanagi, R. Fukaya, S.-I. Adachi, T. Katayama, T. Togashi, S. Owada, M. Yabashi, K. Hatada, A. Iwase, A. Kudo, S. Takakusagi, T. Yokoyama, K. Asakura, Capturing local structure modulations of photoexcited BiVO₄ by ultrafast transient XAFS, Chem. Commun. 53 (2017) 7314–7317.

[38] T. Liu, X. Zhou, M. Dupuisc, C. Li, The nature of photogenerated charge separation among different crystal facets of BiVO₄ studied by density functional theory, Phys. Chem. Chem. Phys. 17 (2015) 23503–23510.

[39] A.J.E. Rettie, W.D. Chemelewski, D. Emin, C.B. Mullins, Unravelling small-polaron transport in metal oxide photoelectrodes, J. Phys. Chem. Lett. 7 (2016) 471–479.

[40] R. Li, F. Zhang, D. Wang, J. Yang, M. Li, J. Zhu, X. Zhou, H. Han, C. Li, Spatial separation of photogenerated electrons and holes among {010} and {110} crystal facets of BiVO₄, Nat. Commun. 4 (2013) 1432.

[41] L. Zhang, Y. Li, X. Li, C. Li, R. Zhang, J.-J. Delaunay, H. Zhu, Solution-processed CuSbS₂ thin film: a promising earth-abundant photocathode for efficient visible-light-driven hydrogen evolution, Nano Energy 28 (2016) 135–142.

[42] M.A. Butler, D.S. Ginley, Prediction of flatband potentials at semiconductor-electrolyte interfaces from atomic electronegativities, J. Electrochem. Soc. 125 (1978) 228–232.

[43] W.-J. Chun, A. Ishikawa, H. Fujisawa, T. Takata, J.N. Kondo, M. Hara, M. Kawai, Y. Matsumoto, K. Domen, Conduction and valence band positions of Ta₂O₅, TaON, and Ta₃N₅ by UPS and electrochemical methods, J. Phys. Chem. B 107 (2003) 1798–1803.